POLITECNICO DI TORINO
Repository ISTITUZIONALE

The impact of process parameters on the lyophilized porous micro-structure: A case study of dextran

Original
The impact of process parameters on the lyophilized porous micro-structure: A case study of dextran / Kosir, A., Artusio, F., Deck, L.-T., Pisano, R., Mazzotti, M.. - In: JOURNAL OF PHARMACEUTICAL SCIENCES. - ISSN 1520-6017. - 114:2(2025), pp. 1434-1443. [10.1016/j.xphs.2024.12.020]

Availability:
This version is available at: 11583/3001680 since: 2025-07-09T10:45:38Z

Publisher:
ELSEVIER

Published
DOI:10.1016/j.xphs.2024.12.020

Terms of use:

This article is made available under terms and conditions as specified in the corresponding bibliographic description in the repository

Publisher copyright

(Article begins on next page)

26 November 2026

Journal of Pharmaceutical Sciences 114 (2025) 1434–1443

Contents lists available at ScienceDirect

Journal of Pharmaceutical Sciences

journal homepage: www.jpharmsci.org

Pharmaceutics, Drug Delivery and Pharmaceutical Technology

The impact of process parameters on the lyophilized porous micro-structure: A case study of dextran

Andraž Košir[a], Fiora Artusio[b], Leif-Thore Deck[a], Roberto Pisano[b], Marco Mazzotti*[,a]

[a] Institute of Energy and Process Engineering, ETH Zurich, 8092 Zurich, Switzerland
[b] Department of Applied Science and Technology, Politecnico di Torino, 10129 Torino, Italy

ARTICLE INFO

Article history:
Received 5 November 2024
Revised 20 December 2024
Accepted 20 December 2024
Available online 31 December 2024

Keywords:
Pharmaceutical manufacturing
Freeze-drying
Image-analysis
Pore size distribution

ABSTRACT

Freeze-drying is used to prolong the shelf life of pharmaceutical formulations stored in vials. To achieve this, formulations are first frozen and then dried, yielding a porous product that can in some cases be stored even at ambient conditions. In this work, the effect of different process parameters on the properties of the porous micro-structure obtained when freeze-drying dextran solutions was studied. To characterize the pore sizes, the samples were imaged with scanning electron microscopy (SEM) and the images were manually analyzed to determine the pore size distribution. To study the robustness of such manual pore characterization methodology, a reliability analysis was carried out, which showed that defining a set of guidelines leads to comparable pore size distributions among multiple participants conducting the analysis. The pore characterization methodology was then applied to products that were freeze-dried under different conditions. Higher dextran concentrations and higher cooling rates were found to lead to predominantly smaller pore sizes and longer primary drying. The conclusions of this work complement the existing literature in demonstrating the robustness of the manual pore size analysis and give valuable insight into the link between the micro-structure formed during the freezing of dextran solutions and the drying performance.
© 2025 The Authors. Published by Elsevier Inc. on behalf of American Pharmacists Association. This is an open access article under the CC BY license (http://creativecommons.org/licenses/by/4.0/)

Introduction

Storing biopharmaceutical formulations in the liquid state often poses a significant risk of potency loss, since the biologically active components of the drug product are prone to various chemical and physical instabilities, such as unfolding and aggregation.[1,2] To mitigate the stability limitations and prolong the shelf life of drug products, freeze-drying (also known as lyophilization) is commonly utilized in the industry.[3–5] In freeze-drying, pharmaceutical formulations stored in vials are first frozen and then dried under vacuum, where ice is removed via sublimation during primary drying and by desorption in the subsequent secondary drying.[3–6] In the freezing stage, a stochastic ice nucleation event marks the first formation of ice, which is followed by fast ice crystal growth (i.e., solidification),[3,4,6–9] and once freezing is completed, drying under vacuum results in a solid material with a complex porous micro-structure.[3,4,10] Due to the complex interplay of freezing and drying, which involves stochastic ice nucleation, heat and mass transfer, and micro-structure formation in the freezing stage – phenomena that affect sublimation and mass transfer during the subsequent drying stage – design and optimization of the freeze-drying process remain challenging.

In particular, the complexity of the freezing stage stems from the fact that both the stochastic ice nucleation and the ensuing solidification contribute to the formation of the ice crystal network and thus determine the properties of the porous micro-structure.[6,10,11] Ice nucleation is an activated process, and denotes the formation of the first primary ice nucleus leading to randomly distributed nucleation times across vials in the same batch, and within the same vial in multiple freeze-thaw cycles.[12] The stochastic nature of nucleation, however, is of relevance not only in the context of freezing in vials[13,14] and droplets,[15,16] but also in the field of crystallization from solution,[17,18] cryopreservation of biological materials such as tissues and cells,[19,20] and in the atmospheric physics.[21,22]

To assess the impact of the different operating conditions on the pore sizes, a reliable micro-structure characterization methodology must be employed. To this end, the specific-surface area of the porous product is often measured,[14,23] or various image-based techniques, such as light microscopy,[24–26] micro computed tomography (μCT),[27–34] and scanning electron microscopy (SEM)[27,34–37] are utilized to characterize the pores. In the present work, SEM imaging was employed due to its availability, comparably high throughput and simple sample preparation, despite the limited information obtained from two-dimensional

* Corresponding author.
E-mail addresses: roberto.pisano@polito.it (R. Pisano), marco.mazzotti@ipe.mavt.ethz.ch (M. Mazzotti).

https://doi.org/10.1016/j.xphs.2024.12.020
0022-3549/© 2025 The Authors. Published by Elsevier Inc. on behalf of American Pharmacists Association. This is an open access article under the CC BY license (http://creativecommons.org/licenses/by/4.0/)

Symbols

γ	cooling rate (°C min^{-1})
w	mass fraction (%)
T	temperature (°C)
p	pressure (Pa)
t	time (min)
D	diameter (m)
A	area (m^2)
k_b	pre-exponential nucleation parameter (m^{-3} s^{-1})
b	exponential nucleation parameter (-)

Subscripts

p	pore
sh	shelf
s	solute
on	the onset of drying curve
mid	the mid-point (inflection point) of drying curve
off	the offset of drying curve
start	denotes the start of drying stage
Pi	Pirani
Ba	Baratron
w	water

Superscripts

eq	equilibrium
nuc	nucleation
dry	drying
end	ending/final value (in context of the minimum shelf temperature)

Abbreviations

SEM	scanning electron microscopy
μCT	micro computed tomography
PDF	probability density function
CV	coefficient of variation
IQR	inter-quartile range
PVDF	polyvinylidene fluoride

images used to determine the pore size distribution. Furthermore, for the image analysis, various automated approaches of pore characterization have been established,[28–30,37,38] however, manual modes of image analysis are nevertheless still used in some cases due to the complexity of identifying pores in the images[14,39] – such an approach is revisited and studied in more detail in this work.

Concerning the role of the porous micro-structure in freeze-drying several potentially relevant aspects remain unclear. First, it is not obvious how different techniques of pore characterization, such as μCT and SEM, compare among each other (while this is not within the scope of this study, an interesting review is found in the literature for the interested readers[39]). More specifically, in the case of SEM image analysis, it is not clear, how different modes of image-analysis, e.g., fully automatic, brightness-based threshold approaches on the one hand, and manual approaches on the other, compare in terms of the obtained pore sizes, or in the case of manual analysis, how the pore size distributions obtained by different participants performing the analysis compare among each other. Second, to further complement the existing literature, there is a need for a better quantitative understanding of how operating conditions and physico-chemical properties of the products relate to pores of different size and morphology, and how these in turn affect the drying performance. For instance, it has been reported that increasing the solute concentration results in smaller pores and thus longer primary drying,[26,30,31,40–44] however, there is a lack of consensus regarding the effect of cooling rate on pore sizes – while some studies report a significant decrease of pore sizes (and/or sublimation rates) when increasing the cooling rate,[24,26,45] others show virtually no effect on pore sizes in the investigated range of cooling rates.[30,42,46]

The present work thus aims to study the complex link between freezing and drying in a quantitative manner in the case of dextran, which is an often used excipient in pharmaceutical formulations (similar in structure to (malto)dextrin, which is also often utilized).[29,47,48] Solute concentration and cooling protocol, together with the time of nucleation, are studied as potential relevant factors affecting the properties of the porous micro-structure (and consequently also the drying time). To characterize the micro-structure, specifically the pore size, samples are imaged with SEM, the pores on the images are manually characterized, and the pore size distribution is determined.

Methodology

Freeze-drying experiments

Materials

Aqueous solutions of dextran (from *Leuconostoc* spp. (40 kDa), purchased from Sigma Aldrich) were prepared with water for injection (Fresenius Kabi, Milan, Italy) in different concentrations (1, 2.5, 5, 10, 15 and 20 wt.%), filtered using syringe filters (PVDF, 0.22 μm, Merck, Milan, Italy), and their water activity was measured at 25 °C using an activity meter (Aqualab TDL 2, METER Group, Inc., Pullman, WA). Physical properties of dextran solutions were taken from the literature,[47,49–51] e.g., the glass transition temperature of the maximally freeze-concentrated solution of dextran, denoted as T'_g, has a value of around −12 °C.[47,48] Dextran solutions were then filled into 10R vials (Stevanato Group, Piombino Dese, Italy) in a laminar flow hood; fill volume in each vial was 3 mL, corresponding to a fill height of 0.95 cm. The vials were then loaded into the freeze-dryer in a 9 × 9 sized hexagonal arrangement, dividing the batch in 49 center vials and 32 edge vials. Freeze-drying experiments were conducted at *Politecnico di Torino* in a lab-scale freeze-dryer LyoBeta 25 (Telstar, Terassa, Spain) with repositioned shelves prior to the start of the first experiment to allow maximum gap between shelves (around 20 cm) and the installation of two HD cameras to monitor the freezing stage. The cameras were then removed from the freeze-dryer before the start of the drying stage, whereas the position of the shelves was kept constant throughout the experimental campaign.

Determining nucleation times

Videos recorded with the two cameras allowed determination of t^{nuc} in all vials, since at t^{nuc} the solution begins to turn from transparent to opaque upon formation of ice. At t^{nuc} the temperature of the product is denoted as T^{nuc}, and represents another freezing characteristics, relevant to describe the conditions of freezing, which can be measured with different invasive and non-invasive methods.[12,52–54] This, nonetheless, was beyond the scope of the present work, where we focus on the determination of nucleation times only.

Experimental protocol

The experimental campaign was divided in two parts (see the experimental conditions summarized in the left part of Table 1): (i) in Exps. A1 to A6, the solute concentration was varied at a constant cooling rate, while (ii) in Exps. B and C, in combination with Exp. A3, the cooling rate was varied at a fixed dextran concentration. All other operating conditions were kept constant. In Exps. A1 to A6 a constant cooling rate, $\gamma = 0.5$ °C min^{-1}, was applied; in Exp. B this value was decreased to 0.2 °C min^{-1}; Exp. C was performed with a pre-cooled shelf to create conditions of faster cooling (temperature of the product as measured with the thermocouple decreased with a rate of approximately 5 °C min^{-1}, see Section S1 in the Supporting Information for further details).

In the case of the shelf-ramped freezing, the shelf temperature was decreased linearly until the minimum temperature, T_{sh}^{end} = −45°C, was reached; vials were then held at the minimum temperature for 3 hours to ensure complete freezing. Afterwards, vacuum was applied and the temperature of the shelf was raised with a heating rate of 1 °C min^{-1} to carry out primary drying at −5 °C. Pressure during primary drying was kept at 10 Pa until the Pirani-Baratron pressure ratio, $p_{Pi}/p_{Ba} \approx 1$, indicated completed primary drying (more details are available in Section 'Determining the endpoint of primary drying'). Finally, the temperature was slowly raised again (with a heating rate of 0.1 °C min^{-1}) to conclude the cycle with a secondary drying stage at the same pressure, but at 20 °C. The duration of the secondary drying step was not optimized and was instead kept constant across experiments. To monitor the temperature evolution of the product, three T-type thermocouples (Tersid, Milan, Italy) were placed in three randomly chosen vials (1 edge and 2 core vials) to monitor the temperature evolution of the product close to the bottom of the vial. An example of the evolution of product temperature (red), shelf temperature (black), and Pirani-Baratron pressure ratio (gray) is shown in Fig. 1 for the case of a 5 wt.% solution of dextran (Exp. A3).

Determining the endpoint of primary drying

The endpoint of primary drying, t^{dry}, was determined based on the Pirani-Baratron ratio, p_{Pi}/p_{Ba}. The Baratron pressure probe is a capacitance manometer, i.e., it provides a composition-independent measurement of the total pressure in the chamber during primary drying; conversely, the Pirani probe is a thermal conductivity gauge, yielding a composition-dependent pressure measurement. The ratio of the two pressure values is therefore also composition-dependent and can be used to detect the endpoint of primary drying – the evolution of p_{Pi}/p_{Ba} is shown in Fig. 1 (gray line), together with multiple points that give indication of the progress of primary drying (i.e., the onset, t_{on}^{dry}, the midpoint, t_{mid}^{dry}, and the offset, t_{off}^{dry}, on the drying curve). The duration of primary drying based on the onset may thus be defined by $\Delta t_{on}^{dry} = t_{on}^{dry} - t_{start}^{dry}$ and analogously based on t_{mid}^{dry} and t_{off}^{dry}. Finally, the change in atmosphere composition ultimately results in the pressure ratio asymptotically approaching a value of $p_{Pi}/p_{Ba} \approx 1$, indicating that the batch of vials is completely dry.[55]

Freeze-dried product characterization

Scanning electron microscopy (SEM) was chosen as the technique to characterize the pores in this work; to this end, multiple center vials in each experiment were selected, namely, two vials associated with each of the 10th, 50th and 90th percentile of the nucleation time distribution were used to probe the effect of the nucleation time on the pore sizes. Conversely, the micro-structure analysis was not carried out for the edge vials.

To prepare the samples for SEM analysis, the vials were first carefully broken, then the product cake was extracted, and, finally, a thin vertical slice of the cake was cut using a razor blade. Samples were then coated with a few nanometers of a Pt layer and 10–20 images from the bulk of the sample (close to the center of the cake in terms of both horizontal and vertical position) were recorded for each sample using SEM (Desktop SEM Phenom XL, Phenom-World B.V., Eindhoven, Netherlands). The obtained SEM images were analyzed manually using *ImageJ*; in each image the identified pores were outlined with a contour of irregular shape and afterwards the build-in software of *ImageJ* was used to compute the pore area, A_p (see Section S3 in the Supporting Information for an example of the image analysis). The circle-equivalent diameter of a pore, D_p, can then be obtained from the pore area using $A_p = \pi D_p^2/4$, in consistency with the literature.[25,26,37] As such, the circle-equivalent diameter of the pores, despite its simplicity and the loss of information about pore shape and orientation, still provides a robust, standardized measure of pore sizes.[39]

SEM image analysis

To render the manual image-analysis more robust, specific guidelines for pore characterization were established before the procedure began. Only completely visible pores should be considered, i.e., not covered by obstructions or artifacts resulting from sample preparation. Furthermore, only pores appearing at the top-most layer of the product (where the sample was cut) should be accounted for, while pores deeper down in the structure should be neglected to avoid double counting, and to achieve reproducible characterization (i.e., counting smaller pores within bigger pores was avoided). Additionally, only pores with a fully visible wall structure at the plane of cutting are to be considered, and all the images were manually examined to avoid double counting of the same pores in potentially overlapping images.

The proposed guidelines were fulfilled for samples of 5 wt.% or higher solute content, whereas samples of 1 and 2.5 wt.% were structurally too weak to be prepared for SEM analysis. The resulting pore structure, as appearing in the images, could not withstand the sample preparation procedure; therefore, these images were not analyzed using the proposed pore size characterization methodology.

Finally, to investigate the reliability of the *manual* pore characterization methodology, five participants analyzed independently the same subset of images – results of this comparison are discussed in Section 'Reliability study of the quantitative analysis of the porous micro-structure'.

Results

Process-level results

Recent studies have established that solute concentration and cooling protocol (e.g., cooling rate) affect the nucleation behaviour of aqueous solutions in vials.[4,6,14,56] The center part of Table 1 shows

Table 1
Table summarizes the main experimental conditions (left), the nucleation time results (middle) and the drying time results (right). Nucleation times are represented by the 10th, 50th (median) and 90th percentile of the nucleation time distribution, whereas drying times are determined by the Pirani-Baratron ratio based on the onset, Δt_{on}^{dry}, the inflection point, Δt_{mid}^{dry}, and the offset of the drying curve, Δt_{off}^{dry}. Nucleation time distributions are reported in the SI (see Section S2).

Experimental conditions				Nucleation time results			Drying time results		
Exp.	cooling mode	γ, [°C min^{-1}]	w_s, [wt.%]	t_{10}^{nuc}, [min]	t_{50}^{nuc}, [min]	t_{90}^{nuc}, [min]	Δt_{on}^{dry}, [h]	Δt_{mid}^{dry}, [h]	Δt_{off}^{dry}, [h]
A1	shelf-ramped freezing	0.5	1	75.7	91.8	104.0	10.4	12.8	15.7
A2			2.5	82.5	98.8	107.7	11.1	14.2	18.2
A3			5	77.6	91.8	104.3	11.0	14.3	17.6
A4			10	85.6	87.8	101.9	12.8	14.4	16.3
A5			15	80.6	96.9	105.6	13.7	16.5	19.9
A6			20	85.3	95.6	105.4	14.0	16.7	20.2
B	shelf-ramped freezing	0.2	5	281.0	305.0	318.3	7.5	11.2	17.3
C	pre-cooled shelf	–	5	4.9	5.5	6.5	8.3	10.2	15.1

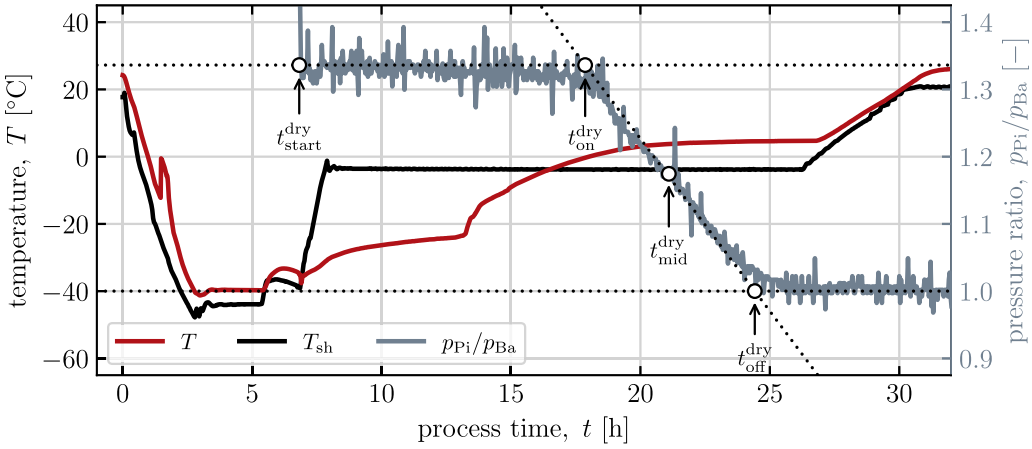


Fig. 1. The evolution of shelf temperature, T_{sh}, (black), product temperature, T, (red) and pressure ratio, p_{Pi}/p_{Ba}, (gray, values on the secondary axis), when freeze-drying a 5 wt.% dextran solution (Exp. A3). The four markers represent the start of primary drying, t^{dry}_{start}, the onset when pressure ratio starts decreasing, t^{dry}_{on}, the mid-point or the inflection point on the ratio curve, t^{dry}_{mid}, and the offset of primary drying, t^{dry}_{off}, when ratio approaches unity. Horizontal dotted lines indicate higher and lower asymptote of p_{Pi}/p_{Ba}, while the third dotted line represents the tangent at t^{dry}_{mid}. Similar plots for other experiments are reported in the SI (see Section S1).

the 10th, 50th and 90th percentiles of nucleation time distribution obtained in each experiment. Nucleation time results in Table 1 show that the percentiles of nucleation time distribution are very similar among experiments with different solute concentration (Exps. A1 to A6), with no clear trend emerging. This implies that in the case of dextran, the solute concentration in the investigated range (1–20 wt.%) has no detectable effect on nucleation. Conversely, recent nucleation study shows that increasing concentrations of sucrose, trehalose and sodium chloride lead to a significant decrease in water activity and thus have a strong impact on the nucleation times and temperatures.[56]

Unlike nucleation times, drying times exhibit a clear and significant trend with respect to solute concentration, as expected based on earlier literature.[26,30,31,40–44] The duration of drying based on the onset of drying, Δt^{dry}_{on}, increased from 10 h to 14 h when freeze-drying 1 and 20 wt.% dextran solution, respectively. A similar increase is observed for the offset of the pressure ratio curve, where the drying time, Δt^{dry}_{off}, increases from 16 h to 20 h.

The effect of the cooling rate on nucleation and drying times can be observed by comparing the results of Exps. B, A3 and C in the bottom part of Table 1. Increasing the cooling rate from 0.2 to 0.5 °C min^{-1} in Exps. A3 and B, respectively, results in shorter nucleation times and longer drying times (Δt^{dry}_{on} increased from 7.5 h to 11 h). Some of the existing literature reports a similar increase in drying times when applying higher cooling rates.[24,26,45,57] This trend, however, is not further observed in Exp. C (pre-cooled shelf), where the drying time is shorter than in Exp. A3, which ran at a cooling rate of 0.5 °C min^{-1}.

To further study the effect of solution composition on the nucleation times, we can define the nucleation rate, J, which represents the expected number of nuclei forming per unit volume and per unit time. It can be defined based on the supersaturation as $J(T) = k_b(a_w - a^{eq}_w(T))^b$, where a_w and a^{eq}_w denote the water activity and the equilibrium water activity, respectively, while k_b and b are constant parameters, which may be estimated from experimental data.[12,56]

Experimental measurements of water activity in dextran solutions, reported in Table 2, show values very similar to that of pure water (i.e., $a_w \approx 1$) for dextran concentrations in the studied range. These values correspond to the literature data even up to 30 wt.%,[58] which means that dextran solutions show negligible freezing-point depression in the investigated solute concentration range. Hence, no relevant effect of dextran concentration on the nucleation rate, and in turn on the measured nucleation times (and thus also nucleation temperatures), is expected.[56] This theoretical consideration is in agreement with the nucleation time data reported in Table 1, where no significant effect of dextran concentration on nucleation times is observed either. However, on the contrary, dextran concentration shows effect on the time of drying, which is investigated through the micro-structure analysis, discussed in the following section.

Micro-structure analysis and pore size results

Qualitative analysis of the porous micro-structure

To facilitate the visual analysis of the porous micro-structure, Fig. 2 shows one SEM image for each of the six experimental conditions studied in this work. All images display the pore structure in the central part of the cake; furthermore, the images are oriented so that the bottom of the image corresponds to a lower vertical position in the freeze-dried product and the top of the image corresponds to a higher vertical position; in other words, the vertical orientation of the sample is preserved in the reported images. For the sake of brevity, only one image per experiment is provided in Fig. 2, whereas many additional SEM images are available in Section S3 of the Supporting Information.

In panels 2a and 2b (Exps. A3 and A4), relatively large and homogeneous pores are observed. A similar pore structure, but with slightly larger pores is also noticed in Fig. 2c (Exp. B). Panels 2d and 2e show samples of images obtained by shelf-ramped freezing in Exps. A5 and A6, which also show a homogeneous pore structure, however, with clearly smaller pore diameters. Finally, Fig. 2f (Exp. C) displays a different morphology of the porous micro-structure. In contrast to the case of slow cooling (Exp. B), where large circular pores with no preferred orientation are observed, in the case of fast cooling with the pre-cooled shelf at –45 °C (Exp. C), narrow channels (i.e., a lamellar structure) in the vertical directions dominate the micro-structure.

The morphology shown in Fig. 2f is characteristic of fast cooling protocols, such as crash-cooling, and is well-known in the literature.[46,59] Fast cooling protocols leading to similar morphology were previously linked to the so-called *local supercooling* in the literature.[46] As opposed to the concept of *global supercooling*, local supercooling means that the product is only supercooled at the time of nucleation in a fraction of its volume.[46,60] In turn, this leads to ice formation upon nucleation only in the supercooled region, whereas elsewhere solidification begins once

Table 2
Measured water activity, a_w, of dextran solutions as a function of solute concentration, w_s, at 25 °C; the mean and the standard deviation of three measurement repetitions is reported.

w_s [wt.%]	a_w [-]
0	0.995 ± 0.003
5	0.992 ± 0.001
10	0.994 ± 0.002
15	0.993 ± 0.001
20	0.990 ± 0.003

the solution reaches the equilibrium freezing temperature locally – interestingly, such a behavior was also predicted in recent modelling works.[60,61]

Panels 2c and 2f clearly demonstrate that different cooling protocols lead to different morphology of the porous micro-structure. A quantitative analysis, however, is challenging in the case of the pre-cooled shelf experiment, due to the lamellar pore structure observed in the SEM images. Instead, a different approach should be used to quantify such lamellar morphology, e.g., based on measuring the width of the vertical channels. Thus, the quantitative pore size analysis was limited only to the conventional shelf-ramped freezing experiments. To assess the reliability of the quantitative results, a specific study as described in the following section was performed.

Reliability study of the quantitative analysis of the porous micro-structure

A set of eleven images belonging to the same sample (one vial with median nucleation time, t_{50}^{nuc}, from Exp. A5) was independently characterized by five participants to assess the reliability and robustness of the characterization methodology explained in Section 'SEM image analysis'. The results are shown in Fig. 3, where panel 3a shows pore sizes estimated from individual images for each operator, while panel 3b shows the resulting pore size distributions for all images together. Each marker in Fig. 3a represents the diameter, D_p, of one pore identified in the corresponding image, n_{im}. Color coding is used to distinguish the results of different participants (represented by letters A to E). For each participant, we combined the results of all images and plotted the resulting pore size distributions in Fig. 3b in the form of a probability density function, f_{D_p}. By definition, $f_{D_p} dD_p$ represents the fraction of pores with a diameter between D_p and $D_p + dD_p$. Furthermore, supporting statistics of the conducted reliability study are highlighted in Table 3.

Both Fig. 3 and Table 3 demonstrate that participants A, B and C identified similar number of pores in the considered dataset (about 230 pores), whereas participants D and E detected a higher number of both smaller and larger pores (428 and 919, respectively). In principle, one may expect that such differences in the number of analyzed pores lead to differences in the resulting pore size distribution, however, Fig. 3b shows comparable pore size distributions characterized by all participants. This is further supported in Table 3, which reports similar average pore sizes, $\overline{D}_p$, and comparable standard deviations,

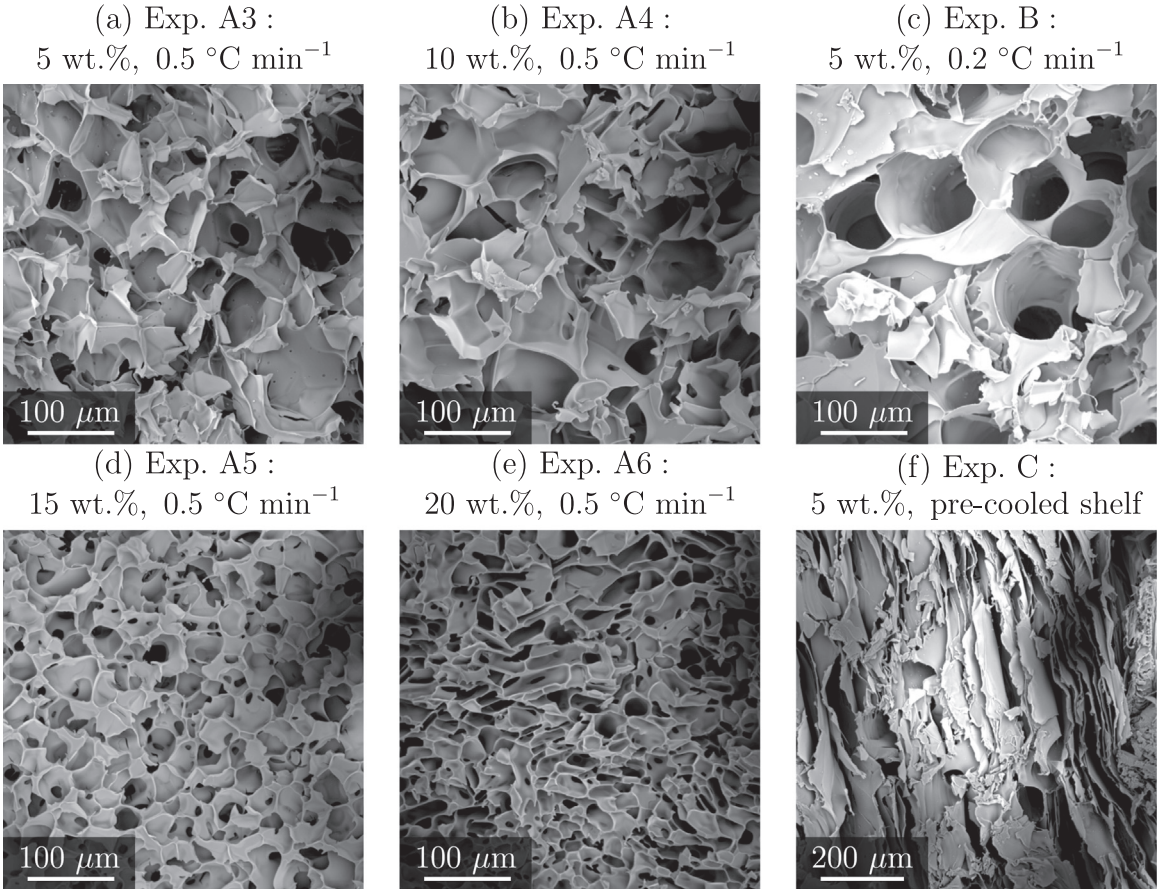


Fig. 2. Representative SEM micrographs of the porous micro-structure obtained in different experiments: (a) Exp. A3, (b) A4, (c) B, (d) A5, (e) A6 and (f) C. Additional SEM images from each experiment are reported in the SI (see Section S3).

σ_p, among all participants – indicating that all participants sampled pore sizes from the same underlying distribution, however, with very different numbers of samples. A detailed examination of individually processed images clarified that participants D and E identified a higher number of pores also in regions of images with lower quality, worse focus and over/under exposure, which were in turn not considered by participants A, B and C. This may be attributed to different interpretation of the predetermined pore characterization guidelines and different adherence to these guidelines. For instance, results for image $n_{im} = 1$ in Fig. 3a show that participants A, B and C identified about 30 pores with sizes 20–50 μm, while participants D and E found overall a higher number of pores, with some of these pores outside the mentioned range. Since all participants measured similar pore size distributions, with participants A, B and C identifying about 200 pores, this implies that essentially around 200 pores constitute a representative sample size that leads to representative pore size distributions (at least in the case of dextran).

All in all, the comparison presented in this section shows that the pore size methodology established in the present work is indeed sufficiently reliable and robust. The methodology was thus applied to samples from other experiments. To decrease the required workload of multiple participants, only participant A analyzed the remaining images.

Quantitative analysis of the porous micro-structure

Quantitative results of the pore characterization are presented in Fig. 4. The pore size distributions are shown as boxplots in Fig. 4a, where the horizontal line within the colored boxes denotes the median pore diameter, while the box height is determined by the first and third quartiles of the distribution, Q_1 and Q_3. The position of the whiskers is given by $Q_1 - 1.5\text{IQR}$ and $Q_3 + 1.5\text{IQR}$, for bottom and top, whereby $\text{IQR} = Q_3 - Q_1$ denotes the interquartile range. Finally, all data points that lie outside of this range are considered outliers and are shown as circles.

Fig. 4a reports three boxplots for each experiment to show the pore size distributions of samples with very different nucleation times. This is represented on the horizontal axis in the form of the nucleation time distribution percentiles, t_x^{nuc}, where x denotes the 10th, 50th and 90th percentile of the nucleation time distribution (the exact values of t_{10}^{nuc}, t_{50}^{nuc} and t_{90}^{nuc} are reported in Table 1 for each experiment).

Let us first consider the effect of cooling rate on the pore sizes. When comparing pore size distributions obtained in Exps. B and A3 (Fig. 4a), a small effect of nucleation time on the pore sizes can be noticed, that is pore sizes in late nucleating vials in Exp. B seem to have slightly smaller pores. However, the same is not observed in case of Exp. A3, where the samples that nucleated close to the median nucleation time show the smallest pore sizes. Furthermore, as observed from Fig. 4b pore sizes slightly increase when slower cooling rate is applied, supporting some of the existing literature in observing that slow cooling leads to larger pores.[3,4,24,26,45] Correspondingly, also the duration of the primary drying stage (see Table 1) decreases in case of slower cooling rate, since larger pores yield lower resistance to mass transfer during drying.

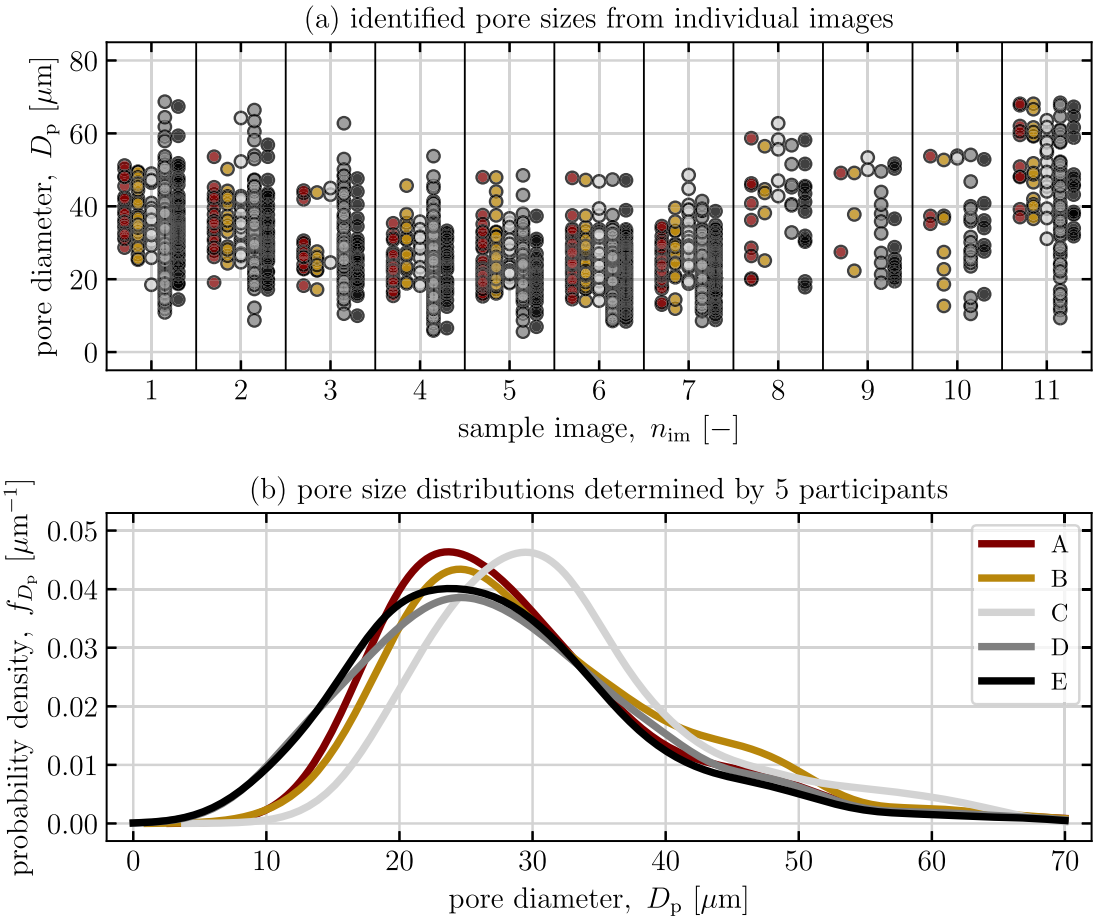


Fig. 3. (a) Each marker indicates a pore identified from one of eleven images, n_{im}, and (b) the resulting pore size distribution, identified by five participants conducting the analysis (represented by letters A, B, C, D and E in color coding). The analyzed images belong to one of the samples with nucleation time close to t_{50}^{nuc} in Exp. A5. Markers in panel (a) are partially transparent to indicate the distribution of pore sizes in the individual images.

Table 3
Summary of the main statistical features of the image analysis for all participants: number of identified pores, N_p, the average pore size, $\overline{D}_p$, the standard deviation, σ_p, as well as the 10th, 50th, and 90th percentiles of the pore size distributions, respectively, are reported.

Participant	N_p [-]	$\overline{D}_p$ [μm]	σ_p [μm]	$D_{p,10}$ [μm]	$D_{p,50}$ [μm]	$D_{p,90}$ [μm]
A	240	29.1	10.2	18.7	27.1	43.3
B	221	30.8	10.6	19.4	28.1	46.3
C	232	32.5	10.1	21.5	30.9	47.0
D	919	28.2	11.1	15.2	26.8	43.0
E	428	27.3	10.5	15.9	25.9	41.1

Regarding the effect of dextran concentration on the pore sizes, Fig. 4a shows a decrease in pore sizes as the solute concentration increases (Exps. A3 to A6), however, no significant trend is observed with respect to nucleation times. This motivates us to concatenate the data of the different nucleation times and to show pore size distributions for the individual experimental conditions, without distinguishing nucleation times. To this end, Fig. 4b shows the pore size distributions for each experiment. First, we recognize that the pore size distribution obtained in Exps. A3 and A4 (i.e., at 5 and 10 wt.% solute concentration) are very similar. Second, similar pore size distributions are also observed for 15 and 20 wt.% dextran concentration, which were used in Exps. A5 and A6. Third, in the case of 5–10 wt.% solute concentration, the average pore sizes range between roughly 60 and 80 μm, whereas for 15 and 20 wt.%, the average pore sizes decrease (roughly by a factor of 2) to about 40 and 55 μm, respectively. Finally, the pore size distribution of 5–10 wt.% products is wider, compared to the higher concentrations.

The measurable effect of dextran concentration on pore sizes demonstrated in Fig. 4 corresponds to the drying times reported in Table 1. Higher solute concentration leads to smaller pore sizes, which in turn translate to longer primary drying.

Hypothesising the role of solute concentration in the micro-structure formation

This section introduces potential explanations for the effect of the solute concentration on the micro-structure of the freeze-dried products. In this context, we emphasize that the experiments reported here were not specifically designed to study the mechanism of micro-structure formation; therefore they cannot provide concluding evidence regarding its exact mechanism. However, the experiments, in particular the use of a video camera to record the freezing process, still provide relevant information.

In agreement with the literature,[4,12,62,63] we observe that the freezing process begins from a single point in space (see Section S5 in the Supplementary Information); before ice formation, the solution is clear, hence this nucleation event is called primary nucleation. Further monitoring reveals that a freezing front (i.e., a macroscopically observed interface of ice and liquid) propagates from the point of primary nucleation and it moves with a rate that depends on dextran concentration. The freezing front in a 10 wt.% solution was found to propagate about twice as fast as in a 20 wt.% solution; it required about 3 and 6 seconds, respectively, to propagate through a fill volume of 3 mL. Finally, following the primary nucleation event and the propagation of the freezing

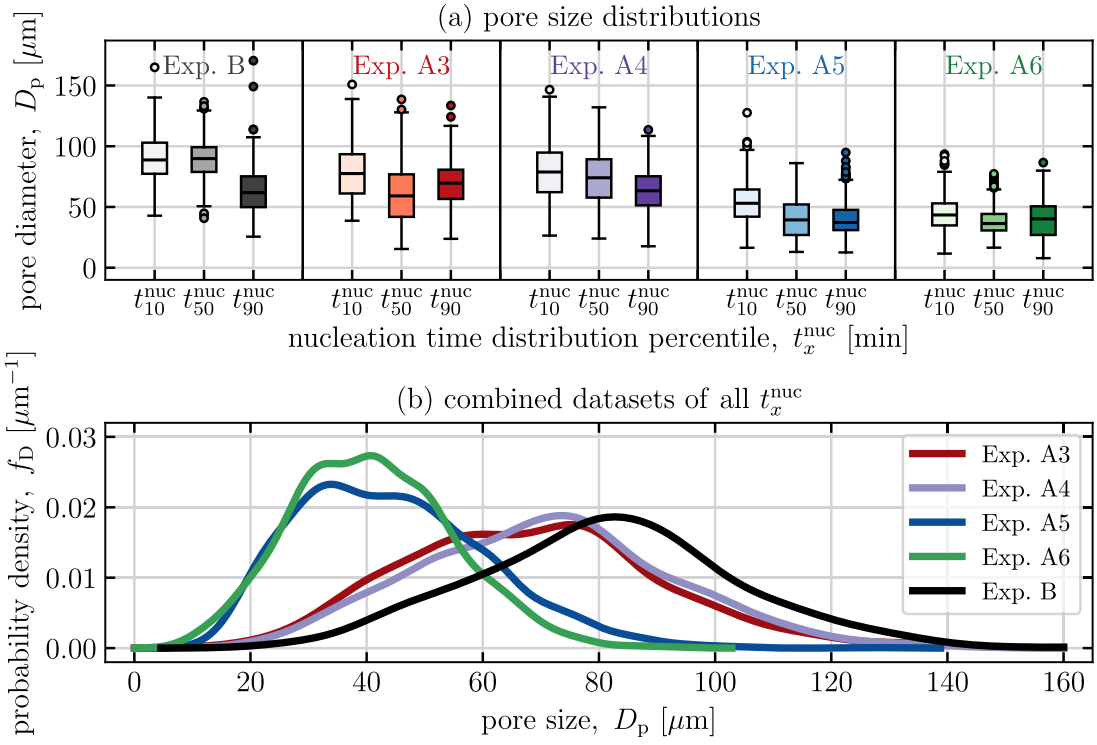


Fig. 4. (a) Pore size distributions in Exps. B, A3, A4, A5 and A6, when considering the effect of nucleation time represented by the different nucleation time distribution percentiles, t_x^{nuc}, on the horizontal axis; (b) total pore size distributions, when combining all pore sizes of specific concentration together, regardless of their nucleation time. Some additional information, such as the number of pores and the coefficients of variations for each boxplot are reported in the SI (see Section S4).

front, further solidification occurs at conditions of low supercooling due to the release of latent heat upon crystallization. In principle, the crystalline micro-structure that evolves into the porous network during drying can originate either from the nucleation stage or from the subsequent solidification stage or a combination of both.

The micro-structure that forms during freezing, however, could not be observed directly, and the only indirect evidence for its existence shown in this work are the SEM images of the dried products. Therefore, we rely on the literature to identify potential mechanisms for its formation. It has been argued that the initial primary nucleation event is followed by rapid crystal growth that results in the formation of a branched, dendritic ice structure;[8,64] alternatively, the propagating freezing front was interpreted as a macro-scopic observation of a large number of crystals formed via secondary nucleation.[46,62,65] Once the freezing front has propagated through the entire volume, the resulting micro-structure then grows further in conditions of low supercooling (again, due to the release of latent heat), which has been associated with the conditions of Ostwald ripening.[66] Furthermore, the rate of ripening scales with the rate of crystal growth; thus, ripening is expected to be slower in more concentrated solutions due to increased solution viscosity,[50,51] implying that the final size of the crystalline structures will be smaller than in more dilute solutions. For instance, the viscosity of 10 wt.% dextran solution is approximately 1.6 times higher than at 5 wt.%, which can potentially explain the observed decrease of crystal growth rate.[51] The effect of dextran concentration (and the related solution viscosity) on the pore sizes is also reflected on the duration of primary drying, corresponding to the existing literature conclusions that increased solute loading leads to smaller pores and thus longer primary drying.[26,30,31,40–42,44]

Given that nucleation, and hence the extent of supercooling at which the ice formation starts, is independent of dextran concentration, the initial properties of the micro-structure may be expected to be concentration-independent as well. Additionally, one might also consider that the solute content affects the specific heat capacity of dextran solutions and the latent heat released during the entire freezing process, however, since we hypothesise that the micro-structure is determined during the fast propagation of the freezing front after nucleation, a minor change in the heat capacity and latent heat is not expected to play a significant role during this period. Nonetheless, it may affect the total ripening (i.e., solidification) time afterwards. More importantly though, considering the mass balance, less water is available in more concentrated solutions, so that the size to which the individual ice crystals (which during drying become pores) can ripe and grow at conditions of low supercooling, would be smaller as well.

It is evident that more work is required to elaborate on the contributions of nucleation, crystal growth, and Ostwald ripening to the formation of the micro-structure during freezing. Regardless of the exact mechanism of micro-structure formation, the results of this study corroborate that the freeze-dried dextran solutions with smaller average pore sizes are associated with a higher resistance to mass transfer during drying, and therefore, slower primary drying.

Conclusions

In this work, the effect of solute composition and cooling protocol on the nucleation and drying times, as well as on the properties of the porous micro-structure is studied for the case of dextran. To characterize the micro-structure, the existing pore characterization methodology based on SEM images was revisited and then a quantitative analysis was applied to determine the pore size distributions.

To be confident in the obtained pore size distributions, a set of images was analyzed by multiple participants to assess the reliability of the manual quantitative analysis. Defining a set of guidelines for pore characterization led to a comparable pore size distribution determined by all participants, independently of their level of training and individual interpretation of the pore characterization guidelines presented in Section 'SEM image analysis'. This prompts us to conclude that the revisited pore size characterization methodology based on SEM images is robust, reliable, and can be used to quantify the effect of various process conditions, such as solute concentration or cooling protocol, on the porous micro-structure in freeze-dried products.

On the one hand, in terms of the process-level results, only minor effect of dextran concentration on nucleation times was observed – a conclusion, which was linked with negligible freezing-point depression of dextran solutions. On the other hand, increasing the solute concentration required longer primary drying stage, which was further confirmed with the micro-structure analysis, since both qualitative and quantitative analysis of the micro-structure showed a decrease in the average pore size as the solute concentration increases. The observed trend was linked to concentration-dependent viscosity, which limits diffusivity of water molecules and leads to smaller average ice crystals. Consequently, smaller pores formed upon sublimation of ice eventually lead to higher resistance to mass transfer during drying, effectively resulting in a longer primary drying. Thus, our results complement the existing studies in the literature and provide further insight into the reliability of manual SEM image-analysis for characterization of freeze-dried products.

Declaration of competing interest

The authors declare that they have no known competing financial interests or personal relationships that could have appeared to influence the work reported in this paper.

Acknowledgments

The authors would like to thank Shina Roshanfekr, Lisanne Wittenberg and Jan Zagar for their effort in the pore characterization study. Furthermore, we would also like to thank Lorenzo Stratta and Claudia Iuliana Udrescu for their support during the research visit at Politecnico di Torino.

Supplementary material

Supplementary material associated with this article can be found in the online version at 10.1016/j.xphs.2024.12.020.

References

1. Rahban M, Ahmad F, Piatyszek MA, Haertlé T, Saso L, Saboury AA. Stabilization challenges and aggregation in protein-based therapeutics in the pharmaceutical industry. *RSC Adv*. 2023;13:35947–35963. https://doi.org/10.1039/D3RA06476J.
2. Izutsu K. *In Survival Strategies in Extreme Cold and Desiccation: Adaptation Mechanisms and Their Applications*. Singapore: Singapore: Springer; 2018:371–383. https://doi.org/10.1007/978-981-13-1244-1_20.
3. Tang XC, Pikal MJ. Design of freeze-drying processes for pharmaceuticals: Practical advice. *Pharm Res*. 2004;21:191–200. https://doi.org/10.1023/B:PHAM.0000016234.73023.75.
4. Assegehegn G, de la, Fuente EB, Franco JM, Gallegos C. The importance of understanding the freezing step and its impact on freeze-drying process performance. *J Pharm Sci*. 2019;108:1378–1395. https://doi.org/10.1016/j.xphs.2018.11.039.
5. Kasper JC, Winter G, Friess W. Recent advances and further challenges in lyophilization. *Eur J Pharm Biopharm*. 2013;85:162–169. https://doi.org/10.1016/j.ejpb.2013.05.019.
6. Kasper JC, Friess W. The freezing step in lyophilization: Physico-chemical fundamentals, freezing methods and consequences on process performance and quality attributes of biopharmaceuticals. *Eur J Pharm Biopharm*. 2011;78:248–263. https://doi.org/10.1016/j.ejpb.2011.03.010.
7. Ryan BF, Wishart ER, Shaw DE. The growth rates and densities of ice crystals between -3°C and -21°C. *J Atmos Sci*. 1976;33:842–850. https://doi.org/10.1175/1520-0469(1976)033<0842:TGRADO>2.0.CO;2.
8. Libbrecht KG. Physical dynamics of ice crystal growth. *Annu Rev Mater Res*. 2017;47:271–295. https://doi.org/10.1146/annurev-matsci-070616-124135.
9. Wahl MS, Aasen A, Hjelme DR, Wilhelmsen O. Ice formation and growth in supercooled water-alcohol mixtures: Theory and experiments with dual fiber sensors. *Fluid Phase Equilib*. 2020;522:112741. https://doi.org/10.1016/j.fluid.2020.112741.

10. Pisano R, Arsiccio A, Nakagawa K, Barresi AA. Tuning, measurement and prediction of the impact of freezing on product morphology: a step toward improved design of freeze-drying cycles. *Drying Technol.* 2019;37:579–599. https://doi.org/10.1080/07373937.2018.1528451.
11. Arsiccio A, Pisano R. The ice-water interface and protein stability: a review. *J Pharm Sci.* 2020;109:2116–2130. https://doi.org/10.1016/j.xphs.2020.03.022.
12. Deck L-T, Mazzotti M. Characterizing and measuring the ice nucleation kinetics of aqueous solutions in vials. *Chem Eng Sci.* 2023;272:118531. https://doi.org/10.1016/j.ces.2023.118531.
13. Deck L-T, Ochsenbein DR, Mazzotti M. Stochastic shelf-scale modeling framework for the freezing stage in freeze-drying processes. *Int J Pharm.* 2021;121276. https://doi.org/10.1016/j.ijpharm.2021.121276.
14. Pisano R, Artusio F, Adami M, et al. Freeze-drying of pharmaceuticals in vials nested in a rack system - Part I: Freezing behaviour. *Pharmaceutics.* 2023;15:2570. https://doi.org/10.3390/pharmaceutics15112570.
15. Koop T, Luo B, Tsias A, Peter T. Water activity as the determinant for homogeneous ice nucleation in aqueous solutions. *Nature.* 2000;406:611–614. https://doi.org/10.1038/35020537.
16. Koop T. Homogeneous ice nucleation in water and aqueous solutions. *Z Phys Chem.* 2004;218:1231–1258. https://doi.org/10.1524/zpch.218.11.1231.50812.
17. Goh L, Chen K, Bhamidi V, et al. A stochastic model for nucleation kinetics determination in droplet-based microfluidic systems. *Cryst Growth Des.* 2010;10:2515–2521. https://doi.org/10.1021/cg900830y.
18. Lambert M, Grossier R, Lagaize M, et al. Modular microfluidic platform for solubility measurement, nucleation statistics and polymorph screening of active pharmaceutical ingredients: Irbesartan, rimonabant, aripiprazole and sulfathiazole. *J Cryst Growth.* 2023;616:127252. https://doi.org/10.1016/j.jcrysgro.2023.127252.
19. Morris GJ, Acton E. Controlled ice nucleation in cryopreservation - a review. *Cryobiology.* 2013;66:85–92. https://doi.org/10.1016/j.cryobiol.2012.11.007.
20. Consiglio AN, Ouyang Y, Powell-Palm MJ, Rubinsky B. An extreme value statistics model of heterogeneous ice nucleation for quantifying the stability of supercooled aqueous systems. *J Chem Phys.* 2023;159:064511. https://doi.org/10.1063/5.0155494.
21. Isenrich FN, Shardt N, Rösch M, et al. The microfluidic ice nuclei counter züurich (MINCZ): a platform for homogeneous and heterogeneous ice nucleation. *Atmos Meas Techn.* 2022;15:5367–5381. https://doi.org/10.5194/amt-15-5367-2022.
22. Marcolli C, Gedamke S, Peter T, Zobrist B. Efficiency of immersion mode ice nucleation on surrogates of mineral dust. *Atmos Chem Phys.* 2007;7:5081–5091. https://doi.org/10.5194/acp-7-5081-2007.
23. Konstantinidis AK, Kuu W, Otten L, Nail SL, Sever RR. Controlled nucleation in freeze-drying: effects on pore size in the dried product layer, mass transfer resistance, and primary drying rate. *J Pharm Sci.* 2011;100:3453–3470. https://doi.org/10.1002/jps.22561.
24. Hottot A, Vessot S, Andrieu J. A direct characterization method of the ice morphology. relationship between mean crystals size and primary drying times of freeze-drying processes. *Drying Technol.* 2004;22:2009–2021. https://doi.org/10.1081/DRT-200032717.
25. Hottot A, Vessot S, Andrieu J. Freeze drying of pharmaceuticals in vials: Influence of freezing protocol and sample configuration on ice morphology and freeze-dried cake texture. *Chem Eng Process Process Intensif.* 2007;46:666–674. https://doi.org/10.1016/j.cep.2006.09.003.
26. Gruber S, Thomik M, Vorhauer-Huget N, Hans L, Tsotsas E, Foerst P. The influence of local microstructure inhomogeneities on local drying kinetics during freeze-drying. *Pharmaceutics.* 2022;14:2132. https://doi.org/10.3390/pharmaceutics14102132.
27. Haeuser C, Goldbach P, Huwyler J, Friess W, Allmendinger A. Imaging techniques to characterize cake appearance of freeze-dried products. *J Pharm Sci.* 2018;107:2810–2822. https://doi.org/10.1016/j.xphs.2018.06.025.
28. Gruber S, Greiner J, Eppink A, et al. Pore shape matters - in-situ investigation of freeze-drying kinetics by 4d XCT methods. *Food Res Int.* 2024;193:114837. https://doi.org/10.1016/j.foodres.2024.114837.
29. Nakagawa K, Tamiya S, Sakamoto S, Do G, Kono S. Observation of microstructure formation during freeze-drying of dextrin solution by in-situ x-ray computed tomography. *Front Chem.* 2018;6:418. https://doi.org/10.3389/fchem.2018.00418.
30. Foerst P, de M, Carvalho T, et al. Estimation of mass transfer rate and primary drying times during freeze-drying of frozen maltodextrin solutions based on x-ray μ-computed tomography measurements of pore size distributions. *J Food Eng.* 2019;260:50–57. https://doi.org/10.1016/j.jfoodeng.2019.05.002.
31. Thomik M, Gruber S, Kaestner A, Foerst P, Tsotsas E, Vorhauer-Huget N. Experimental study of the impact of pore structure on drying kinetics and sublimation front patterns. *Pharmaceutics.* 2022;14:1538. https://doi.org/10.3390/pharmaceutics14081538.
32. Vanbillemont B, Lammens J, Goethals W, Vervaet C, Boone MN, De Beer T. 4d micro-computed x-ray tomography as a tool to determine critical process and product information of spin freeze-dried unit doses. *Pharmaceutics.* 2020;12:430. https://doi.org/10.3390/pharmaceutics12050430.
33. Lammens J, Goudarzi NM, Leys L, et al. Spin freezing and its impact on pore size, tortuosity and solid state. *Pharmaceutics.* 2021;13:2126. https://doi.org/10.3390/pharmaceutics13122126.
34. Izutsu K, Yonemochi E, Yomota C, Goda Y, Okuda H. Studying the morphology of lyophilized protein solids using x-ray micro-CT: effect of post-freeze annealing and controlled nucleation. *AAPS PharmSciTech.* 2014;15:1181–1188. https://doi.org/10.1208/s12249-014-0152-5.
35. Sitar A, Skrlec K, Voglar J, et al. Effects of controlled nucleation on freeze-drying lactose and mannitol aqueous solutions. *Drying Technol.* 2018;36:1263–1272. https://doi.org/10.1080/07373937.2017.1399903.
36. Perepezko J, Wilde G. Melt undercooling and nucleation kinetics. *Curr Opin Solid State Mater Sci.* 2016;20:3–12. https://doi.org/10.1016/j.cossms.2015.07.001.
37. Arsiccio A, Sparavigna AC, Pisano R, Barresi AA. Measuring and predicting pore size distribution of freeze-dried solutions. *Drying Technol.* 2019;37:435–447. https://doi.org/10.1080/07373937.2018.1430042.
38. Hojat N, Gentile P, Ferreira AM, Siller L. Automatic pore size measurements from scanning electron microscopy images of porous scaffolds. *J Porous Mater.* 2023;30:93–101. https://doi.org/10.1007/s10934-022-01309-y.
39. Bartoš M, Suchý T, Foltán R. Note on the use of different approaches to determine the pore sizes of tissue engineering scaffolds: what do we measure? *Biomedical Engineering Online.* 2018;17:110. https://doi.org/10.1186/s12938-018-0543-z.
40. Pikal M, Shah S, Senior D, Lang J. Physical chemistry of freeze-drying: Measurement of sublimation rates for frozen aqueous solutions by a microbalance technique. *J Pharm Sci.* 1983;72:635–650. https://doi.org/10.1002/jps.2600720614.
41. Raman P. Freeze drying microscopy as a tool to study sublimation kinetics. 2015. Ph.D thesis, Loughborough University, U.K. https://hdl.handle.net/2134/18316.
42. Ray P, Rielly CD, Stapley AG. A freeze-drying microscopy study of the kinetics of sublimation in a model lactose system. *Chem Eng Sci.* 2017;172:731–743. https://doi.org/10.1016/j.ces.2017.05.047.
43. Arsiccio A, Barresi AA, Pisano R. Prediction of ice crystal size distribution after freezing of pharmaceutical solutions. *Cryst Growth Des.* 2017;17:4573–4581. https://doi.org/10.1021/acs.cgd.7b00319.
44. Pikal MJ. *In Encyclopedia of Pharmaceutical Technology: Volume 3 (3rd ed.).* CRC Press; 2007:1807–1834. https://www.routledge.com/Encyclopedia-of-Pharmaceutical-Technology-Volume-6/Swarbrick/p/book/9780429132728.
45. Voda A, Homan N, Witek M, et al. The impact of freeze-drying on microstructure and rehydration properties of carrot. *Food Res Int.* 2012;49:687–693. https://doi.org/10.1016/j.foodres.2012.08.019.
46. Searles JA, Carpenter JF, Randolph TW. The ice nucleation temperature determines the primary drying rate of lyophilization for samples frozen on a temperature-controlled shelf. *J Pharm Sci.* 2001;90:860–871. https://doi.org/10.1002/jps.1039.
47. Haeuser C, Goldbach P, Huwyler J, Friess W, Allmendinger A. Impact of dextran on thermal properties, product quality attributes, and monoclonal antibody stability in freezedried formulations. *Eur J Pharm Biopharm.* 2020;147:45–56. https://doi.org/10.1016/j.ejpb.2019.12.010.
48. Larsen BS, Skytte J, Svagan AJ, Meng-Lund H, Grohganz H, Löbmann K. Using dextran of different molecular weights to achieve faster freeze-drying and improved storage stability of lactate dehydrogenase. *Pharm Dev Technol.* 2019;24:323–328. https://doi.org/10.1080/10837450.2018.1479866.
49. Kawaizumi F, Nishio N, Nomura H, Miyahara Y. Calorimetric and compressibility study of aqueous solutions of dextran with special reference to hydration and structural change of water. *Polym J.* 1981;13:209–213. https://doi.org/10.1295/polymj.13.209.
50. Tirtaatmadja V, Dunstan DE, Boger DV. Rheology of dextran solutions. *J Non-Newtonian Fluid Mech.* 2001;97:295–301. https://doi.org/10.1016/S0377-0257(00)00226-3.
51. Gonzalez-Castillo C, Rubio R, Zenteno-Savin T. Coronary flow-induced inotropism is modulated by binding of dextrans to the endothelial luminal surface. *Am J Physiol-Heart Circ Physiol.* 2003:284. https://doi.org/10.1152/ajpheart.00323.2002.
52. Lietta E, Colucci D, Distefano G, Fissore D. On the use of infrared thermography for monitoring a vial freeze-drying process. *J Pharm Sci.* 2019;108:391–398. https://doi.org/10.1016/j.xphs.2018.07.025.
53. Jiang X, Kazarin P, Sinanis MD, et al. A non-invasive multipoint product temperature measurement for pharmaceutical lyophilization. *Sci Rep.* 2022;12:12010. https://doi.org/10.1038/s41598-022-16073-x.
54. Deck L-T, Ferru N, Košir A, Mazzotti M. Visualizing and understanding batch heterogeneity during freeze-drying using shelf-scale infrared thermography. *Ind Eng Chem Res.* 2024;63:16335–16346. https://doi.org/10.1021/acs.iecr.4c02215.
55. Patel SM, Doen T, Pikal MJ. Determination of end point of primary drying in freeze-drying process control. *AAPS PharmSciTech.* 2010;11:73–84. https://doi.org/10.1208/s12249-009-9362-7.
56. Deck L-T, Wittenberg L, Mazzotti M. Thermodynamics explains how solution composition affects the kinetics of stochastic ice nucleation. *J Phys Chem Lett.* 2023;14:5993–6000. https://doi.org/10.1021/acs.jpclett.3c01371.
57. Goshima H, Do G, Nakagawa K. Impact of ice morphology on design space of pharmaceutical freeze-drying. *J Pharm Sci.* 2016;105:1920–1933. https://doi.org/10.1016/j.xphs.2016.04.001.
58. De Vito F, Veytsman B, Painter P, Kokini JL. Simulation of the effect of hydrogen bonds on water activity of glucose and dextran using the Veytsman model. *Carbohydr Polym.* 2015;117:236–246. https://doi.org/10.1016/j.carbpol.2014.09.024.
59. Zhang H, Cooper AI. Aligned porous structures by directional freezing. *Adv Mater.* 2007;19:1529–1533. https://doi.org/10.1002/adma.200700154.
60. Deck L-T, Košir A, Mazzotti M. Modeling the freezing process of aqueous solutions considering thermal gradients and stochastic ice nucleation. *Chem Eng J.* 2024;483:148660. https://doi.org/10.1016/j.cej.2024.148660.
61. Chen G, Kong W, Wang L, Wang F. On the experimental and theoretical model for ice crystal characteristics near a substrate. *Int J Heat Mass Transf.* 2020;152:119462. https://doi.org/10.1016/j.ijheatmasstransfer.2020.119462.
62. Capozzi LC, Pisano R. Looking inside the 'black box': Freezing engineering to ensure the quality of freeze-dried biopharmaceuticals. *Eur J Pharm Biopharm.* 2018;129:58–65. https://doi.org/10.1016/j.ejpb.2018.05.020.

63. Wenzel T, Gieseler M, Gieseler H. Design of vacuum-induced freezing protocols for high fill volume formulations in freeze-drying: a strategic approach. *J Pharm Sci*. 2020;109:3035–3044. https://doi.org/10.1016/j.xphs.2020.06.025.
64. Rodrigues MA, Miller MA, Glass MA, Singh SK, Johnston KP. Effect of freezing rate and dendritic ice formation on concentration profiles of proteins frozen in cylindrical vessels. *J Pharm Sci*. 2011;100:1316–1329. https://doi.org/10.1002/jps.22383.
65. Geidobler R, Winter G. Controlled ice nucleation in the field of freeze-drying: Fundamentals and technology review. *Eur J Pharm Biopharm*. 2013;85:214–222. https://doi.org/10.1016/j.ejpb.2013.04.014.
66. van Westen T, Groot RD. Predicting the kinetics of ice recrystallization in aqueous sugar solutions. *Cryst Growth Des*. 2018;18:2405–2416. https://doi.org/10.1021/acs.cgd.8b00038.